

Frequency-bin entangled comb of photon pairs from a Silicon-on-Insulator micro-resonator

Jun Chen,^{1,2*} Zachary H. Levine,¹ Jingyun Fan,^{1,2}
and Alan L. Migdall^{1,2}

¹ *Optical Technology Division, National Institute of Standards and Technology
100 Bureau Drive, Gaithersburg, MD 20899-8441, USA*

² *Joint Quantum Institute, University of Maryland, College Park, MD 20742, USA*

[*jun.chen@nist.gov](mailto:jun.chen@nist.gov)

Abstract: We present a quantum-mechanical theory to describe narrow-band photon-pair generation via four-wave mixing in a Silicon-on-Insulator (SOI) micro-resonator. We also provide design principles for efficient photon-pair generation in an SOI micro-resonator through extensive numerical simulations. Microring cavities are shown to have a much wider dispersion-compensated frequency range than straight cavities. A microring with an inner radius of 8 μm can output an entangled photon comb of 21 pairwise-correlated peaks (42 comb lines) spanning from 1.3 μm to 1.8 μm . Such on-chip quantum photonic devices offer a path toward future integrated quantum photonics and quantum integrated circuits.

OCIS codes: (190.4380) Nonlinear optics, four-wave mixing; (190.4390) Nonlinear optics, integrated optics; (270.5585) Quantum information processing; (230.5750) Resonators; (230.3990) Micro-optical devices.

References and links

1. D. Bouwmeester, A. K. Ekert, and A. Zeilinger, *The Physics of Quantum Information: Quantum Cryptography, Quantum Teleportation, Quantum Computation*, 1st Ed., (Springer 2000).
2. P. G. Kwiat, K. Mattle, H. Weinfurter, A. Zeilinger, A. V. Sergienko, and Y. Shih, "New High-Intensity Source of Polarization-Entangled Photon Pairs," *Phys. Rev. Lett.* **75**, 4337 (1995).
3. T. E. Kiess, Y. H. Shih, A. V. Sergienko, and C. O. Alley, "Einstein-Podolsky-Rosen-Bohm Experiment Using Pairs of Light Quanta Produced by Type-II Parametric Down-conversion," *Phys. Rev. Lett.* **71**, 3893 (1993).
4. M. Fiorentino, P. L. Voss, J. E. Sharping, and P. Kumar, "All-fiber photon-pair source for quantum communications," *IEEE Photon. Technol. Lett.* **14**, 983 (2002).
5. H. Takesue and K. Inoue, "Generation of polarization-entangled photon pairs and violation of Bell's inequality using spontaneous four-wave mixing in a fiber loop," *Phys. Rev. A* **70**, 031802(R) (2004).
6. X. Li, P. L. Voss, J. E. Sharping, and P. Kumar, "Optical-Fiber Source of Polarization-Entangled Photons in the 1550 nm Telecom Band," *Phys. Rev. Lett.* **94**, 053601 (2005).
7. J. Fan, A. Migdall, and L. J. Wang, "Efficient generation of correlated photon pairs in a microstructure fiber," *Opt. Lett.* **30**, 3368 (2005).
8. J. G. Rarity, J. Fulconis, J. Duligall, W. J. Wadsworth, and P. S. Russell, "Photonic crystal fiber source of correlated photon pairs," *Opt. Express* **13**, 534 (2005).
9. A. Politi, M. J. Cryan, J. G. Rarity, S. Yu, and J. L. O'Brien, "Silica-on-Silicon waveguide quantum circuits," *Science* **320**, 646 (2008).
10. A. Mohan, M. Felici, P. Gallo, B. Dwir, A. Rudra, J. Faist, and E. Kapon, "Polarization-entangled photons produced with high-symmetry site-controlled quantum dots," *Nature Photon.* **4**, 302 (2010).
11. K. Banaszek, A. B. U'Ren, and I. A. Walmsley, "Generation of correlated photons in controlled spatial modes by downconversion in nonlinear waveguides," *Opt. Lett.* **26**, 1367 (2001).

12. M. Fiorentino, S. M. Spillane, R. G. Beausoleil, T. D. Roberts, P. Battle, and M. W. Munro, "Spontaneous parametric down-conversion in periodically poled KTP waveguides and bulk crystals," *Opt. Express* **15**, 7479 (2007).
13. J. Chen, A. Pearlman, A. Ling, J. Fan, and A. Migdall, "A versatile waveguide source of photon pairs for chip-scale quantum information processing," *Opt. Express* **17**, 6727 (2009).
14. T. Zhong, F. N. C. Wong, T. D. Roberts, and P. Battle, "High performance photon-pair source based on a fiber-coupled periodically poled KTiOPO₄ waveguide," *Opt. Express* **17**, 12019 (2009).
15. J. E. Sharping, K. F. Lee, M. A. Foster, A. C. Turner, B. S. Schmidt, M. Lipson, A. L. Gaeta, and P. Kumar, "Generation of correlated photons in nanoscale silicon waveguides," *Opt. Express* **14**, 12388 (2006).
16. K. Harada, H. Takesue, H. Fukuda, T. Tsuchizawa, T. Watanabe, K. Yamada, Y. Tokura, and S. Itabashi, "Generation of high-purity entangled photon pairs using silicon wire waveguide," *Opt. Express* **16**, 20368 (2008).
17. S. Clemmen, K. P. Huy, W. Bogaerts, R. G. Baets, Ph. Emplit, and S. Massar, "Continuous wave photon pair generation in silicon-on-insulator waveguides and ring resonators," *Opt. Express* **17**, 16558 (2009).
18. P. P. Absil, J. V. Hryniewicz, B. E. Little, P. S. Cho, R. A. Wilson, L. G. Joneckis, and P.-T. Ho, "Wavelength conversion in GaAs micro-ring resonators," *Opt. Lett.* **25**, 554 (2000).
19. A. C. Turner, M. A. Foster, A. L. Gaeta, and M. Lipson, "Ultra-low power parametric frequency conversion in a silicon microring resonator," *Opt. Express* **16**, 4881 (2008).
20. Q. Lin and G. P. Agrawal, "Silicon waveguides for creating quantum-correlated photon pairs," *Opt. Lett.* **31**, 3140 (2006).
21. H. J. Kimble, "The quantum internet," *Nature* **453**, 1023 (2008).
22. J. Chen, X. Li, and P. Kumar, "Two-photon-state generation via four-wave mixing in optical fibers," *Phys. Rev. A* **72**, 033801 (2005).
23. Q. Lin, O. J. Painter, and G. P. Agrawal, "Nonlinear optical phenomena in silicon waveguides: Modeling and applications," *Opt. Express* **15**, 16604 (2007).
24. We note that the optical modes in our proposed microring resonators are not ideal whispering gallery modes, in the sense that the modes have non-zero interaction with the inner wall of the ring resonators. However, the electric field strength at the inner wall is typically no more than 1% of its peak value near the outer wall (see Fig. 2). Even though this interaction is negligibly small, we used the numerically determined modes in our calculations, rather than analytical expressions of ideal whispering gallery modes. We still refer to our modes as whispering gallery modes throughout the text, but we recognize this is an approximation.
25. M. Scholtz, L. Koch, O. Benson, "Analytical treatment of spectral properties and signal-idler intensity correlations for a double-resonant optical parametric oscillator far below threshold," *Opt. Commun.* **282**, 3518 (2009).
26. J. Brendel, N. Gisin, W. Tittel, and H. Zbinden, "Pulsed energy-time entangled twin-photon source for quantum communication," *Phys. Rev. Lett.* **82**, 2594 (1999).
27. C. K. Law, I. A. Walmsley, and J. H. Eberly, "Continuous frequency entanglement: effective finite Hilbert space and entropy control," *Phys. Rev. Lett.* **84**, 5304 (2000).
28. S. Ramelow, L. Ratschbacher, A. Fedrizzi, N. K. Langford, and A. Zeilinger, "Discrete tunable color entanglement," *Phys. Rev. Lett.* **103**, 253601 (2009).
29. L. Orlislager, J. Cussey, A. T. Nguyen, P. Emplit, S. Massar, J.-M. Merolla, and K. Phan Huy, "Frequency-bin entangled photons," *Phys. Rev. A* **82**, 013804 (2010).
30. L. Yin, Q. Lin, and G. P. Agrawal, "Dispersion tailoring and soliton propagation in silicon waveguides," *Opt. Lett.* **31**, 1295 (2006).
31. A. C. Turner, C. Manolatou, B. S. Schmidt, M. Lipson, M. A. Foster, J. E. Sharping, and A. L. Gaeta, "Tailored anomalous group-velocity dispersion in silicon channel waveguide," *Opt. Express* **14**, 4357 (2006).
32. A. C. Turner-Foster, M. A. Foster, R. Salem, A. L. Gaeta, and M. Lipson, "Frequency conversion over two-thirds of an octave in silicon nanowaveguides," *Opt. Express* **18**, 1904 (2010).
33. M. Heiblum and J. H. Harris, "Analysis of curved optical waveguides by conformal transformation," *IEEE J. Quantum Electron.* **11**, 75 (1975).
34. E. D. Palik, *Handbook of Optical Constants of Solids*, (Academic Press 1985), p. 548.
35. <http://www.comsol.com>
36. Certain trade names and company products are mentioned in the text or identified in an illustration in order to specify adequately the experimental procedure and equipment used. In no case does such identification imply recommendation or endorsement by the National Institute of Standards and Technology, nor does it necessarily imply that the products are the best available for the purpose.
37. Q. Lin, T. J. Johnson, R. Perahia, C. P. Michael, and O. J. Painter, "A proposal for highly tunable optical parametric oscillation in silicon micro-resonators," *Opt. Express* **16**, 10596 (2008).
38. I. H. Agha, Y. Okawachi, M. A. Foster, J. E. Sharping, and A. L. Gaeta, "Four-wave-mixing parametric oscillations in dispersion-compensated high-Q silica microspheres," *Phys. Rev. A* **76**, 043837 (2007).
39. M. Oxborrow, "Traceable 2-D finite-element simulation of the whispering-gallery modes of axisymmetric electromagnetic resonators," *IEEE Tran. Micro. Theory* **55**, 1209 (2007).
40. Private communications with M. Oxborrow and P. Del'Haye.

1. Introduction

Quantum-entangled photon pairs play a key role in quantum information processing applications such as quantum key distribution, quantum teleportation, and linear optical quantum computing [1]. Traditional sources produce such photon pairs using spontaneous parametric down conversion (SPDC) in bulk $\chi^{(2)}$ nonlinear crystals [2, 3], and more recently, spontaneous four-wave mixing (FWM) in $\chi^{(3)}$ standard optical fibers [4–6] and photonic crystal fibers [7, 8]. However, the common drawback for all these sources is that they do not offer an easy path to scalable integration. As quantum optical circuits become increasingly complex to handle more and more qubits, it is highly desirable to develop a compact and efficient way to produce and propagate photonic qubits while preserving quantum coherence among them. Silica-on-Silicon waveguide quantum circuits [9] have emerged as an efficient *passive* guide for single photons. On the other hand, compact *active* devices for generating photon pairs demonstrated so far include quantum dots [10], SPDC in quasi-phase-matched microphotonic waveguides [11–14], and FWM in Silicon-on-Insulator (SOI) nanophotonic straight waveguides [15, 16] and microring resonators [17]. Among these, SOI devices appear most integration-compatible by leveraging the mature Si fabrication technology from the integrated circuit industry. As the bending loss decreases exponentially with increasing core-cladding refractive index difference, the high index contrast between crystalline Si and its surroundings (air and/or SiO₂) enable ultrasmall bending radii (several μm) without incurring high loss, thus enabling large-density integration of SOI devices in a single platform.

Both SOI straight waveguides and microring resonators are of great interest: the former are capable of generating broadband FWM photon pairs, whereas the latter output narrowband photons. Classically, the field enhancement effect by a microring resonator has been studied in Ref. [18] with GaAs microring resonators, and in Ref. [19] with SOI microring resonators. Quantum mechanically, there are several experimental demonstrations of photon pair generation in straight SOI waveguides [15, 16], and a quantum theoretical description has also appeared [20]. For microring resonators, Ref. [17] demonstrates photon pair generation experimentally, but uses classical arguments from Ref. [18] to explain their experimental results which leads to certain discrepancies. This highlights the need for a quantum theory for describing resonator-enhanced photon-pair generation in SOI micro-cavities, which we present in Section 2. Our theory is also markedly different from the straight-waveguide quantum theory in Ref. [20] in that our theory deals with FWM in a resonant cavity while Ref. [20] treats FWM in a non-resonant structure, with the emission bandwidth from the former being at least 3 orders of magnitude narrower than the latter. This helps address the issue of mode-mismatch between photonic and material qubit systems by narrowing the difference in inherent bandwidths, which is now an area of much research interest [21]. In addition, instead of using Heisenberg picture with operator evolution as done in Ref. [20], our theory uses Schrödinger picture with state vector evolution, which facilitates explicit calculation of the final two-photon wave function and spectral characteristics. Section 3 is devoted to discussing important design principles for SOI microring resonators developed through extensive numerical modelling. Straight-cavity resonators are studied in Section 4, and are found to be generally inferior to their ring-shaped counterparts in terms of enhancing FWM photon-pair production. We conclude with an outlook for future work in Section 5.

2. Quantum theory of two-photon state generation via cavity-enhanced four-wave mixing

FWM is a third-order [$\chi^{(3)}$] nonlinear process, in which 2 pump photons are absorbed and a pair of energy- and momentum-conserving daughter photons (referred to as signal and idler) are generated, satisfying $2\omega_p = \omega_s + \omega_i$ and $2\vec{k}_p = \vec{k}_s + \vec{k}_i$, where $\omega_{p,s,i}$ and $\vec{k}_{p,s,i}$ are the photon

frequencies and wavevectors, and the subscripts p, s, and i stand for pump, signal, and idler, respectively. Here we focus on a continuous-wave (CW) pump scenario, which is also the most relevant pumping scheme for a micro-resonator cavity. A treatment of the pulsed-pump case can be done by following Ref. [22]. Emitted simultaneously as a pair, signal and idler photons are strongly time-energy entangled, forming a two-photon state.

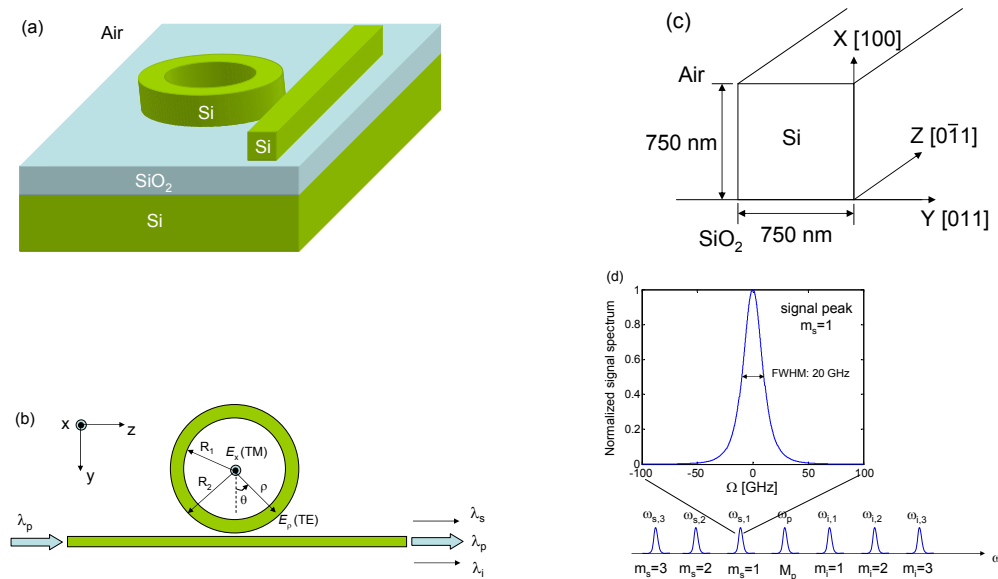


Fig. 1. (a) Schematic of a microring resonator side-coupled to a bus waveguide, both integrated on a SOI chip. (b) Top-down view of photon pair production in the SOI device shown in (a). Pump is injected into the microring via the bus waveguide; copolarized photon pairs are generated and resonantly enhanced and evanescently coupled out of the microring. Waves propagate in the z direction in the bus waveguide. Inside the microring, there exist two polarization eigenmodes: TM (Electric field perpendicular to the plane of propagation) and TE (Electric field in the plane of propagation but perpendicular to the propagation direction). R_1 , inner ring radius; R_2 , outer ring radius. (c) Cross section of both the microring and the bus waveguide. The crystallographic axes are designated for the bus waveguide only. (d) An entangled comb of photon pairs is generated when pump frequency is tuned to mode number M_p . A signal photon occupying mode m_s can always find its partner idler photon symmetrically placed around pump occupying mode $m_i = m_s$. Also shown is the simulated signal output with a relative mode number $m_s = 1$, which has a full width at half-maximum of 20 GHz for a cavity damping rate of 31.25 GHz.

The integrated SOI devices under consideration consist of a microring side-coupled to a straight bus waveguide [Fig. 1(a)]. The bus waveguide can be fabricated on the same chip, but it can also be a tapered optical fiber. The coupling strength between the two can be tuned by changing their separation, which also tunes the cavity damping rate γ . Strong, CW pump light at λ_p is injected into the microring from the bus waveguide [Fig. 1(b)]. The wavelength λ_p is chosen to be near the zero-dispersion wavelength λ_{ZDW} of the microring (or equivalently, a bent waveguide) so that FWM phase matching produces a broad gain spectrum without taking into account the cavity resonances. The resonator effectively acts like an active filter, enhancing its resonant frequencies while suppressing all other non-resonant ones.

For simplicity we focus on the case where both the microring and the bus waveguide share the same cross-sectional dimensions. This monolithic design will minimize spatial mode mis-

match between the microring and the bus waveguide if the bending radius is not too small. The cross section is shown in Fig. 1(c), where a 750 nm by 750 nm square-shaped Si block sits on top of a SiO₂ buried oxide (BOX) layer (with a thickness $\geq 0.5\ \mu\text{m}$ to prevent leakage into the Si substrate) with an air top cladding. The bus waveguide is fabricated along the $[0\ \bar{1}\ 1]$ direction on a (1 0 0) silicon wafer for cleaving convenience. This particular geometry is chosen because numerical simulations show that the microring's zero-dispersion wavelengths for both quasi-TE [transverse electric, E_ρ in Fig. 1(b)] and quasi-TM [transverse magnetic, E_x in Fig. 1(b)] fundamental modes are within the 1550 nm telecommunications band (see Section 3). Although shown as a ring, the microcavity could also be shaped as a racetrack to improve coupling between the resonator and the bus waveguide. Both the microring and the bus waveguide are multimode over a broad spectral range due to the deep etch down to the BOX layer; however, higher-order modes have quite different spatial mode profiles, polarization, and dispersion characteristics compared to the fundamental modes. As a result, FWM involving higher-order modes have negligible contributions to the production of correlated photon pairs inside the wavelength range of interest. Thus we can limit our study of the generation of photon pairs to fundamental modes only.

There are a myriad of nonlinear optical processes that may occur when intense pump light circulates around the SOI microring. These include FWM, Raman scattering, Brillouin scattering, two-photon absorption (TPA), and free carrier absorption (FCA). A general description of these processes can be found in Ref. [23]. For the purpose of generating photon pairs, we are concerned only with spontaneous FWM, as the pump power is kept low to avoid stimulated scattering. Processes such as TPA and FCA are only efficient when the pump power is high, and therefore can be neglected in the low pump power regime. Brillouin scattering is two orders of magnitude weaker in strength compared with first-order Raman scattering in Si [23], and therefore is negligible here. Due to the intrinsic crystal symmetry of Si and the ring structure under consideration, Raman scattering is absent for the process wherein a quasi-TM pump transfers its energy to another quasi-TM mode (TM-TM), but is allowed for all other processes such as TM-TE, TE-TM, and TE-TE to transfer part of the pump energy to a mode that is 15.6 THz down-shifted from the pump (the so-called Stokes wave) with a full width at half-maximum (FWHM) of 105 GHz [23]. Thanks to the narrow-band nature of Raman scattering in Si, it is possible to neglect Raman scattering altogether by simply designing the microring cavity to have its resonances detuned from the pump-derived Raman Stokes wave (see Section 3 for details).

The following theory is developed with general applicability to all cavities, including straight cavities and microring cavities as special cases. The notation, however, uses that of a straight cavity as default. When applied to a microring cavity, care should be taken as there are subtleties of whispering gallery modes (WGM) [24] that are not entirely captured in the following formalism. For example, the physical length L of a straight cavity mode remains fixed, while for the microring WGMs it shortens slightly for shorter resonant wavelengths. Another example is the transverse mode overlap between optical fields, which for straight cavity modes can be assumed to be close to unity, but for WGMs it is generally less than 1 because the mode profiles shift slightly with wavelength. Nevertheless, for signal and idler wavelengths close to the pump the above differences are minute, and can be safely disregarded.

The physical cavity length L is typically several tens of micrometers long. We further require that all optical fields participating in the FWM process are fundamental resonant modes of the cavity, satisfying: $n_{gj}L = M_j\lambda_j$ ($j=p, s, i$), where M_j are integer mode numbers ($M_s < M_p < M_i$) and n_{gj} are group indices for each field. The propagation direction is denoted as z (which should be replaced by $\rho\theta$ for the microring case). Without loss of generality, the transverse spatial mode of each field is taken to be the fundamental TM mode of the cavity, and we assume that

all fields are copolarized so that scalar notation can be used. The pump field is a classical wave:

$$E_p^{(+)}(z, t) = E_p e^{i[k_p(\omega_p)z - \omega_p t]} e^{-i\Gamma P z}, \quad (1)$$

where Γ is the nonlinear parameter for the Si waveguide and P is the circulating power inside the cavity. Note that the pump self-phase modulation term $e^{-i\Gamma P z}$ is explicitly included. The resonant signal field is quantized, and can be written as [25]:

$$E_s^{(-)}(z, t) = \sqrt{\frac{\hbar \omega_s}{2\epsilon_0 n_s c A_{\text{eff},s}}} \frac{\sqrt{\gamma_s \Delta \omega_s}}{2\pi} \sum_{m_s} \int_{-\infty}^{\infty} d\Omega_s \frac{a_s^\dagger(\omega_{s,m_s} + \Omega_s)}{\gamma_s/2 - i\Omega_s} e^{-i[k_s z - (\omega_{s,m_s} + \Omega_s)t]}. \quad (2)$$

The idler equation can be obtained by exchanging the subscripts s and i . Here $A_{\text{eff},s} = |\iint |F_s|^2 dx dy|^2 / \iint |F_s|^4 dx dy$ is the effective mode area, with F_s being the transverse mode profile of the signal field. γ_s is the cavity damping rate for the signal, which represents all possible loss mechanisms including both linear loss (propagation loss, out-coupling loss) and nonlinear loss (TPA, FCA). In practice, the nonlinear loss terms play a minor role at the pump power levels we use (see Section 3 for loss estimation). $\Delta \omega_s$ is the free spectral range (FSR), ω_{s,m_s} is the m_s th central frequency, Ω_s is the deviation from ω_{s,m_s} , and a_s^\dagger is the creation operator for signal. Lastly, we use *positive* integers $m_s = M_p - M_s$ and $m_i = M_i - M_p$ to represent the *relative* mode number for signal and idler, respectively.

Using first-order perturbation theory, the two-photon state $|\Psi\rangle = (i\hbar)^{-1} \int_{-\infty}^{\infty} dt H_I |0\rangle$ can be calculated through the interaction Hamiltonian $H_I = \zeta \chi^{(3)} \int_{-L}^0 dz E_p^{(+)} E_p^{(+)} E_s^{(-)} E_i^{(-)} + h.c.$ where ζ is a proportionality constant, and *h.c.* stands for Hermitian conjugate. For simplicity, we only consider signal and idler frequencies close to the pump, so that a Taylor expansion of the propagation constant k around the pump frequency can be employed, and we keep the expansion series up to second order (k''). A straightforward calculation yields the following expression for the two-photon state:

$$|\Psi\rangle = \eta L \sum_{m_s} \sum_{m_i} \int_{-\infty}^{\infty} d\Omega_s \int_{-\infty}^{\infty} d\Omega_i \frac{\sqrt{\gamma_s \gamma_i} \delta(-m_s \Delta \omega_s + m_i \Delta \omega_i + \Omega_s + \Omega_i)}{(\gamma_s/2 - i\Omega_s)(\gamma_i/2 - i\Omega_i)} e^{iL \left[\frac{k''}{4} (m_s \Delta \omega_s - \Omega_s)^2 + \frac{k''}{4} (m_i \Delta \omega_i + \Omega_i)^2 + \Gamma P \right]} a_s^\dagger(\omega_{s,m_s} + \Omega_s) a_i^\dagger(\omega_{i,m_i} + \Omega_i) |0\rangle \text{sinc} \left\{ L \left[\frac{k''}{4} (m_s \Delta \omega_s - \Omega_s)^2 + \frac{k''}{4} (m_i \Delta \omega_i + \Omega_i)^2 + \Gamma P \right] \right\}, \quad (3)$$

where η is another proportionality constant, and $k'' = \frac{d^2 k}{d\omega^2} |_{\omega=\omega_p}$ is the group velocity dispersion at the pump frequency ω_p . In deriving Eq. (3), we have used the following mathematical identities:

$$\int_{-\infty}^{\infty} e^{iut} dt = 2\pi \delta(u), \quad (4)$$

$$\int_{-L}^0 e^{-i\beta x} dx = L e^{i\beta L/2} \text{sinc}(\beta L/2). \quad (5)$$

We can further simplify Eq. (3) by taking into account the following reasonable assumptions: (i) the cavity bandwidth is much smaller than the FSR ($|\Omega_{s(i)}| \ll \Delta \omega_{s(i)}$) and (ii) all participating frequencies are close so that there is negligible difference in their group indices and the FSR

can be considered constant ($m_s = m_i = m$, $\Omega_s = -\Omega_i = \Omega$, $\Delta\omega_s = \Delta\omega_i = \Delta\omega$). The following simplified two-photon state is thus obtained:

$$|\Psi\rangle = \eta L \sum_m \int_{-\infty}^{\infty} d\Omega \frac{\sqrt{\gamma_s \gamma_i} e^{iL[k''(m\Delta\omega - \Omega)^2/2 + \Gamma P]}}{(\gamma_s/2 - i\Omega)(\gamma_i/2 + i\Omega)} \text{sinc}\{L[k''(m\Delta\omega - \Omega)^2/2 + \Gamma P]\} a_s^\dagger(\omega_p - m\Delta\omega + \Omega) a_i^\dagger(\omega_p + m\Delta\omega - \Omega) |0\rangle. \quad (6)$$

Equation 6 demonstrates the energy-entangled nature of the two-photon state through the arguments of its two creation operators (which sum up to twice the pump frequency). The two-photon state also exhibits a “frequency-bin entangled comb” structure with discrete spectral peaks that are correlated pairwise in energy, all in a superposition state. The frequency-bin entanglement notion is exactly analogous to time-bin entanglement [26] as a discrete form of the more familiar continuous frequency entanglement [27]. Photon pairs in Eq. (6) can be thought of as existing in discrete “Schmidt modes” [27]: If one photon is found to be in the mode $|\omega_p - m\Delta\omega + \Omega\rangle$, then its partner must be found in the mode $|\omega_p + m\Delta\omega - \Omega\rangle$. The “comb” term signifies the nearly equidistant nature of these mode pairs when the dispersion in the cavity is low (or compensated). We emphasize that the frequency-bin entangled state introduced here is different from the ones recently demonstrated in Ref. [28] (two-level frequency-entangled qubits) and Ref. [29] (discrete, one-to-many frequency correlation). In comparison, our state features *multi-level, one-to-one* frequency correlation with explicitly-generated (instead of mathematically decomposed) Schmidt mode pairs.

Although simplified, Eq. (6) is still useful in most practical cases, and can be used to calculate the biphoton production rate ($\sim \langle \Psi | \Psi \rangle$), the single-photon spectrum, and the coincidence spectrum. We calculate the single-photon spectrum below as an example. The spectrum of signal photons is obtained via $S(\omega_s) = \langle \Psi | a_s^\dagger(\omega_s) a_s(\omega_s) | \Psi \rangle$. Using Eq. (6), we obtain:

$$S(\omega_s) = (\eta L)^2 \sum_m \frac{\gamma_s \gamma_i \text{sinc}^2\{L[k''(\omega_p - \omega_s)^2/2 + \Gamma P]\}}{|\gamma_s/2 - i(\omega_s - \omega_p + m\Delta\omega)|^2 |\gamma_i/2 + i(\omega_s - \omega_p + m\Delta\omega)|^2}. \quad (7)$$

The idler photon spectrum can be derived in a similar fashion:

$$\begin{aligned} S(\omega_i) &= \langle \Psi | a_i^\dagger(\omega_i) a_i(\omega_i) | \Psi \rangle \\ &= (\eta L)^2 \sum_m \frac{\gamma_s \gamma_i \text{sinc}^2\{L[k''(\omega_i - \omega_p)^2/2 + \Gamma P]\}}{|\gamma_s/2 - i(\omega_p - \omega_i + m\Delta\omega)|^2 |\gamma_i/2 + i(\omega_p - \omega_i + m\Delta\omega)|^2}. \end{aligned} \quad (8)$$

We can see that the single-photon spectrum is defined by two frequency characteristics that are wildly different. First of all, the sinc function defines the frequency range in which the FWM phase matching condition is satisfied. It can extend to almost 100 THz for some cases (see Fig. 5 for examples). On the other hand, the product of the two Lorentzians (a characteristic of the cavity) defines the narrow-band output of each resonant peak under the sinc-function envelope. Comparison between Eq. (7) and Eq. (8) leads to the observation that signal and idler spectra consist of identically-shaped spectral peaks that are pairwise energy-entangled, forming an entangled photon comb. Idler damping (γ_i) plays a role in shaping the signal spectrum, and vice versa. Each comb peak has a FWHM that is related to the cavity damping rate through: $\text{FWHM} = \sqrt{\sqrt{2} - 1} \gamma \approx 0.64\gamma$, where we assume $\gamma_s = \gamma_i = \gamma$. A numerically simulated signal peak for $m_s = 1$ is shown in Fig. 1(d), where $\gamma = 31.25$ GHz is assumed (which leads to a resonant peak FWHM of 20 GHz).

3. Design principles of SOI microring resonators

A microring resonator has several key design parameters: the cross section dimensions and the bending curvature (quantified by the ring inner radius R_1). All of them dramatically affect

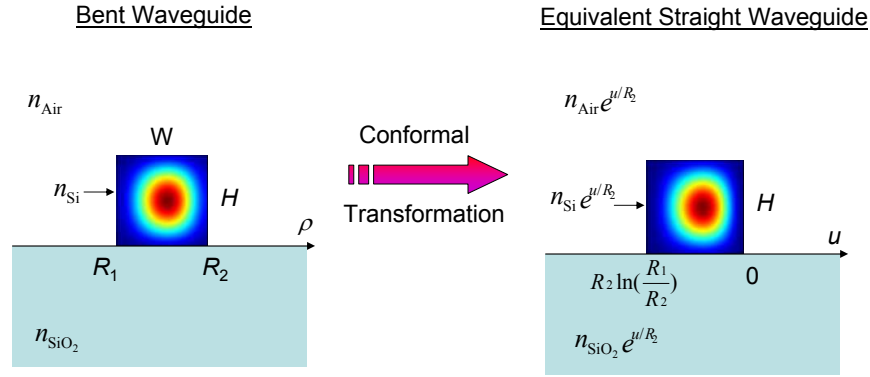


Fig. 2. Conformal transformation from a bent waveguide to its equivalent straight waveguide, along with the fundamental TE mode shape ($R_1 = 8 \mu\text{m}$, $\lambda = 1.528 \mu\text{m}$) in its corresponding coordinate.

the microring's dispersion properties, and in particular its zero-dispersion wavelength, which has significant implications on where the pump wavelength should be. The effect of the cross section (both size and aspect ratio) on the dispersion of a straight Si waveguide has been studied extensively [30–32]. However, the effect of the bending curvature on dispersion has not been fully explored, to the best of our knowledge. Here we take the ring's cross section to be fixed at $750 \text{ nm} \times 750 \text{ nm}$, and gradually change R_1 (from ∞ for a straight waveguide to $3 \mu\text{m}$) to find its effect on the microring dispersion.

The microring is modelled as a bent waveguide, and a conformal transformation approach is used to transform the bent waveguide to its equivalent straight waveguide [33]. The procedure is illustrated in Fig. 2, where the conformal transformation is described by

$$u = R_2 \ln(\rho/R_2), \quad (9)$$

$$v = R_2 \theta. \quad (10)$$

Here ρ and θ are polar coordinates depicted in Fig. 1(b), with $\rho = \sqrt{y^2 + z^2}$ and $\theta = \arctan(z/y)$ (y, z are Cartesian coordinates). v is the direction of propagation (perpendicular to the cross section in Fig. 2). As shown in Fig. 2, a bent waveguide with inner (outer) radius R_1 (R_2), width $W \equiv R_2 - R_1$, and height H is transformed to an equivalent straight waveguide of width $-R_2 \ln(R_1/R_2)$ and height H . The refractive index of each material is also transformed according to $n'_a = n_a e^{u/R_2}$, $a = \text{Air, Si, SiO}_2$. For the refractive indices, we use

$$n_{\text{Air}} = 1, \quad (11)$$

$$n_{\text{SiO}_2} = \sqrt{1 + \frac{0.6961663 \lambda^2}{\lambda^2 - 0.0684043^2} + \frac{0.4079426 \lambda^2}{\lambda^2 - 0.1162414^2} + \frac{0.8974794 \lambda^2}{\lambda^2 - 9.896161^2}}, \quad (12)$$

$$n_{\text{Si}} = 3.41906 + \frac{0.123172}{\lambda^2 - 0.028} + \frac{0.0265456}{(\lambda^2 - 0.028)^2} - 2.66511 \times 10^{-8} \lambda^2 + 5.45852 \times 10^{-14} \lambda^4, \quad (13)$$

where we have used the Sellmeier equations for air and SiO_2 , and the Herzberger equation for Si [34]. λ is the free-space wavelength in units of micrometers. Note that the equivalent straight waveguide is situated in the negative- u plane.

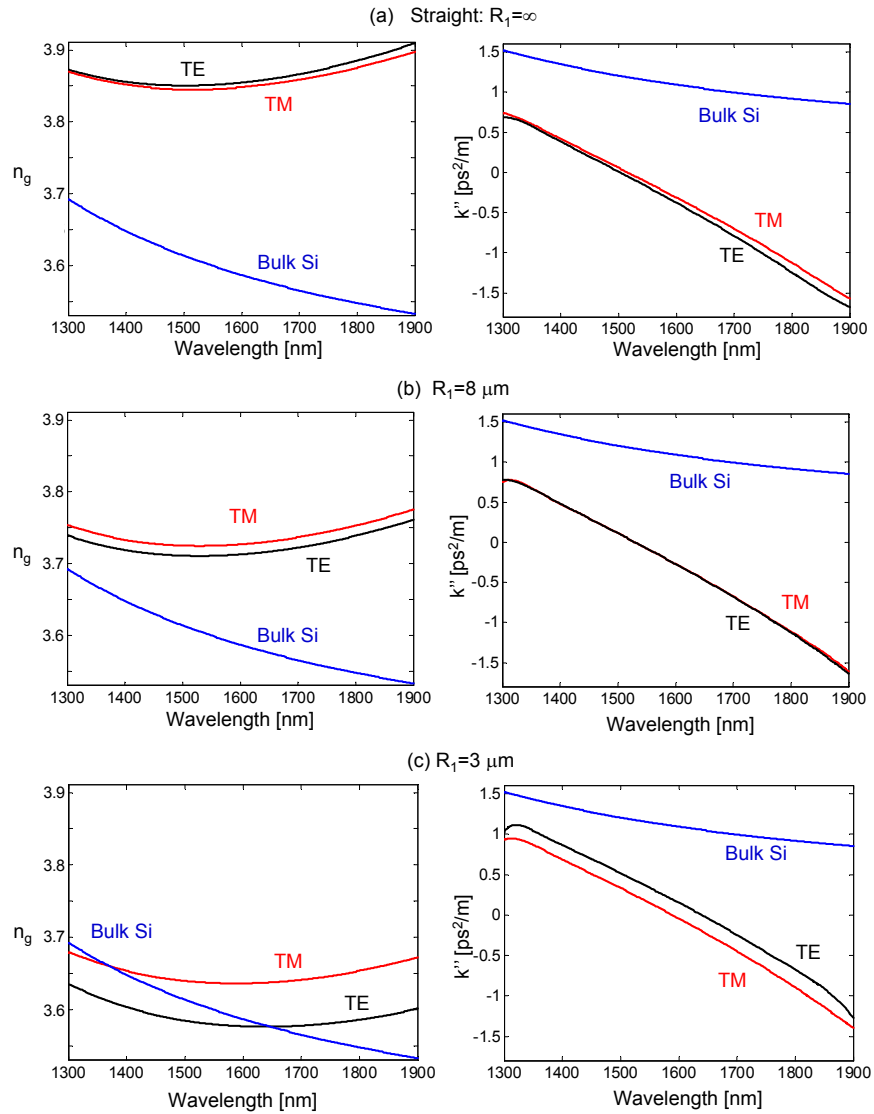


Fig. 3. Numerically simulated group index n_g and group velocity dispersion k'' for (a) straight waveguide, (b) bent waveguide with $R_1 = 8 \mu\text{m}$, and (c) bent waveguide with $R_1 = 3 \mu\text{m}$. TE mode: black; TM mode: red. The curves for bulk Si are plotted in blue for reference.

We use a commercial finite-element solver (COMSOL [35, 36]) to numerically calculate the eigenmodes and propagation constants for each waveguide, from which we obtain the group index ($n_g = c \frac{dk}{d\omega}$) and the group velocity dispersion ($k'' = \frac{d^2k}{d\omega^2}$) through numerical differentiation, where c is the vacuum speed of light. The results are shown in Fig. 3, for a straight waveguide and two bent waveguides with its inner radius $R_1 = 8 \mu\text{m}$ and $3 \mu\text{m}$, respectively. Bending the waveguide has a significant influence on both the group index and group velocity dispersion of its fundamental TE and TM modes. Bending a straight waveguide to $R_1 = 8 \mu\text{m}$ changes the relative magnitude of the group index for TE and TM modes, and a further bend-

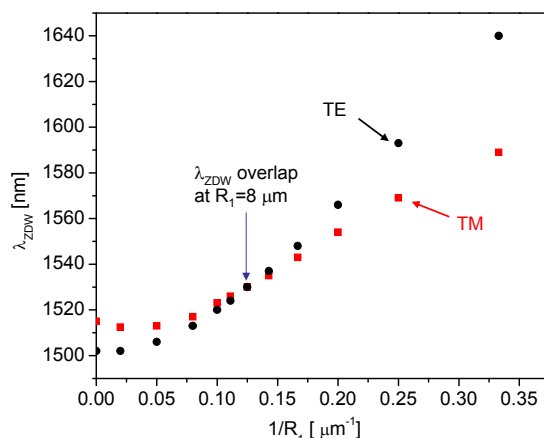


Fig. 4. Zero-dispersion wavelength vs. the inverse of the bending radius of an SOI waveguide for both TE (black dots) and TM (red squares) modes.

ing to $R_1 = 3 \mu\text{m}$ reverses the relative positions of the group velocity dispersion curves for TE and TM modes. The bending effect on dispersion is more pronounced when R_1 becomes comparable to the waveguide cross dimension ($0.75 \mu\text{m}$ in this case).

The above bending effect can be intuitively understood if we notice from Fig. 2 that the equivalent straight waveguide has a smaller index contrast ($\Delta n' = \Delta n e^{u/R_2}$) than a straight waveguide ($\Delta n = n_{\text{Si}} - n_{\text{surroundings}}$) for $u \leq 0$, where the mode is predominantly located. Furthermore, $\Delta n'$ reduces with decreasing R_1 (or R_2). This means that mode confinement is strongest for a straight waveguide; as the bending increases (R_1 decreases), the mode confinement becomes weaker. Therefore, both group index and group velocity dispersion approach that of bulk Si with decreasing R_1 , as can be seen in Fig. 3.

Since the zero-dispersion wavelength (λ_{ZDW}) is of great interest for phase-matching considerations, we plot its dependence on the inverse of the bending curvature ($1/R_1$) in Fig. 4. We can see that the bending curvature has a dramatic effect on the location of zero-dispersion wavelengths for both TE and TM modes. At a suitable bending radius ($R_1 = 8 \mu\text{m}$), the TE and TM zero-dispersion wavelengths overlap ($\lambda_{\text{ZDW}}^{\text{TE}} = \lambda_{\text{ZDW}}^{\text{TM}} = 1530 \text{ nm}$). This can also be seen in Fig. 3(b), as the TE and TM k'' curves almost completely overlap each other throughout the wavelength range from 1300 nm to 1900 nm. At a small bending radius of $R_1 = 3 \mu\text{m}$, $\lambda_{\text{ZDW}}^{\text{TE}}$ far exceeds $\lambda_{\text{ZDW}}^{\text{TM}}$ by over 50 nm. We also see that bending affects TE modes more than TM modes, as the slope for $\lambda_{\text{ZDW}}^{\text{TE}}$ vs. $1/R_1$ is larger than that for $\lambda_{\text{ZDW}}^{\text{TM}}$ vs. $1/R_1$. This is because TE polarization is within the bending plane, while TM polarization is perpendicular to it, making the two polarizations see the bending effect differently. The above information can help us determine where the optimal pump wavelength should be for a microring resonator of a given size, as can be seen in the next part of our simulation.

For an azimuthally symmetric resonator such as a microring, each resonant WGM mode exhibits a unique angular momentum with a field distribution of $E_M(\rho, \theta, x) \sim e^{iM\theta}$ where M is an integer [see Fig. 1(b)]. The FWM phase-matching requirement of linear momentum conservation in a straight geometry is adapted to angular momentum conservation in a curved geometry, which stipulates $2M_p = M_s + M_i$. This is clearly satisfied for signal/idler pairs that are symmetrically placed around the pump mode, i.e., $M_{s/i} = M_p \pm m$ (m is an integer). Due to the dispersion inside the microring, the equally-important energy conservation requirement is not

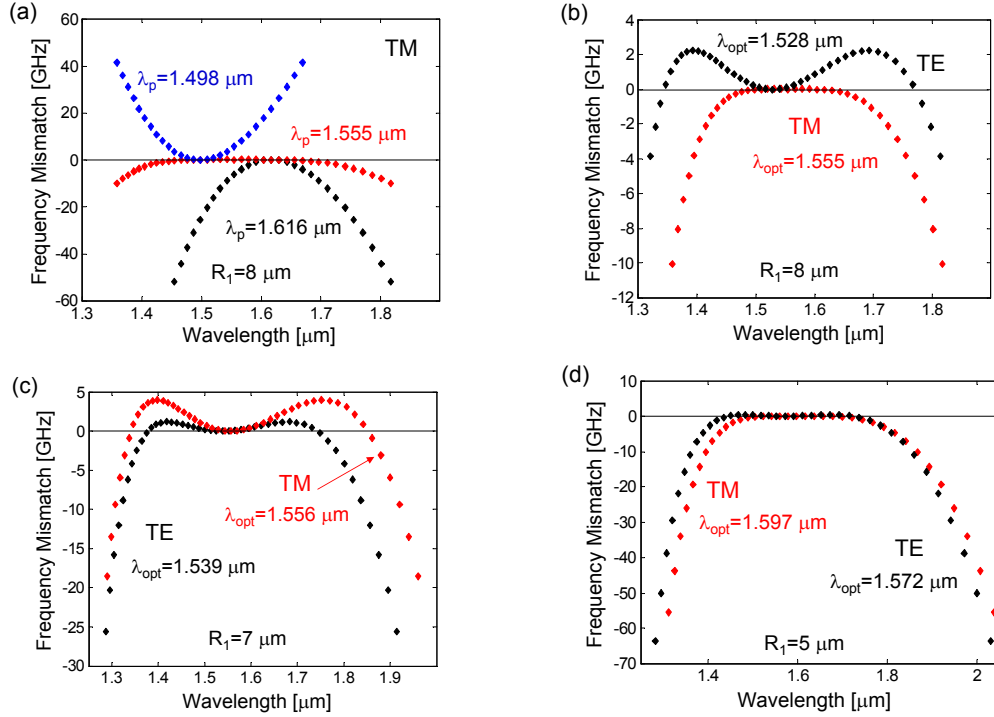


Fig. 5. (a) Frequency mismatch for TM modes for a microring resonator of $R_1 = 8 \mu\text{m}$. Blue, $\lambda_p = 1.498 \mu\text{m}$ with $M_p = 114$; red, $\lambda_p = 1.555 \mu\text{m}$ with $M_p = 109$; black, $\lambda_p = 1.616 \mu\text{m}$ with $M_p = 104$. One can see that $M_p = 109$ corresponds to the optimal pump mode. Frequency mismatch when pump is chosen optimally for TE (black) and TM (red) for several different bending radii: (b) $R_1 = 8 \mu\text{m}$, $M_p = 111$ for TE, $M_p = 109$ for TM; (c) $R_1 = 7 \mu\text{m}$, $M_p = 97$ for TE, $M_p = 96$ for TM; and (d) $R_1 = 5 \mu\text{m}$, $M_p = 69$ for TE, $M_p = 68$ for TM. Optimal pump wavelengths are labelled on the figures.

always satisfied for those adjacent modes, which is quantified by the *frequency mismatch* [37]:

$$\Delta = \frac{1}{2\pi} (2\omega_{0p} - \omega_{0s} - \omega_{0i}), \quad (14)$$

where ω_{0j} ($j = p, s, i$) are resonant frequencies of the microring. It is clear that if all optical fields participating in FWM are resonant modes of the cavity, the FWM efficiency will be greatly enhanced. Therefore, it is important to reduce the frequency mismatch to below the cavity linewidth, in which case the FWM efficiency will suffer the least (referred to as the dispersion-compensated regime in Ref. [38]). For each R_1 , we numerically simulate the resonant modes using the weak-form formulation in COMSOL developed by Oxborrow [39]. An iterative routine is needed to arrive at self-consistent resonances when the wavelength-dependent refractive indices of SiO_2 and Si (cf. Eqs. 12 and 13) are taken into account [40]. Frequency mismatch is then calculated via Eq. (14) for various pump wavelengths.

Typical results are shown in Fig. 5 for several values of the bending radii. For $R_1 = 8 \mu\text{m}$, Fig. 5(a) shows that there is an optimal pump for which frequency mismatch is minimized over a large wavelength range (from $1.3 \mu\text{m}$ to $1.8 \mu\text{m}$), which we denote as λ_{opt} . Any deviation from the optimal pump results in reduction of the effective FWM range. As shown in Fig. 5(b), TM and TE modes generally have different λ_{opt} , even though for $R_1 = 8 \mu\text{m}$ they have the

same zero-dispersion wavelength: for TM mode $\lambda_{\text{opt}} = 1.555 \mu\text{m}$, and for TE mode $\lambda_{\text{opt}} = 1.528 \mu\text{m}$. Nevertheless, both are very close to $\lambda_{\text{ZDW}} = 1530 \text{nm}$, with negligible k'' values ($k'' = -0.097 \text{ps}^2/\text{m}$ for TM and $k'' = 0.005 \text{ps}^2/\text{m}$ for TE). Extensive numerical study shows that this statement holds true for other bending radii as well; Fig. 5(c) and (d) depict two such examples. For $R_1 = 7 \mu\text{m}$, Fig. 5(c) shows that $\lambda_{\text{opt}} = 1.556 \mu\text{m}$ with $k'' = -0.08 \text{ps}^2/\text{m}$ for TM and $\lambda_{\text{opt}} = 1.539 \mu\text{m}$ with $k'' = -0.007 \text{ps}^2/\text{m}$ for TE. Figures 5(d) depicts the case for $R_1 = 5 \mu\text{m}$, where we have $\lambda_{\text{opt}} = 1.597 \mu\text{m}$ with $k'' = -0.17 \text{ps}^2/\text{m}$ for TM and $\lambda_{\text{opt}} = 1.572 \mu\text{m}$ with $k'' = -0.026 \text{ps}^2/\text{m}$ for TE. In all these examples, the optimal pump resides close to λ_{ZDW} , and often (but not always) in the anomalous dispersion regime (i.e., $k'' < 0$).

Take an SOI microring with $R_1 = 8 \mu\text{m}$ for example. From Fig. 5(b) we can see that the effective FWM range is roughly estimated to be $[1.3 \mu\text{m}, 1.8 \mu\text{m}]$, where the frequency mismatch $|\Delta| \leq 4 \text{GHz}$ for TE modes and $|\Delta| \leq 10 \text{GHz}$ for TM modes. Inside this 500-nm broad wavelength range, there exist 21 TE-comb and 19 TM-comb peak pairs. Each peak has a FWHM of 20 GHz, and peaks are separated by a free spectral range of about 12 nm. These are important design parameters that are relevant for experimentally testing a fabricated device.

In addition to the linear frequency mismatch in Eq. (14), there is a nonlinear contribution to frequency mismatch due to the intensity-dependent refractive index [38], which is given by

$$\Delta_{\text{nl}} = \frac{2n_2 I \omega_p}{n(\omega_p) 2\pi}, \quad (15)$$

where $n_2 = 2.5 \times 10^{-18} \text{m}^2/\text{W}$ is the nonlinear index coefficient of Si and I is the intensity of the pump circulating the cavity. Assuming a pump circulating power of 100 mW inside the microring (very high for the purpose of photon-pair production) and an effective area $A_{\text{eff}} = 0.33 \mu\text{m}^2$, the intensity I is estimated to be about $3 \times 10^{11} \text{W}/\text{m}^2$. Δ_{nl} is then estimated to be 86 MHz at a wavelength of 1550 nm, which is much less than the cavity linewidth (20 GHz, corresponding to a moderate cavity Q of 10^4). Therefore, the nonlinear contribution to frequency mismatch can be ignored for most practical cases.

Let us also estimate the product ΓPL_{eff} , which is important in gauging the importance of nonlinear loss terms such as TPA and FCA. According to the studies done in Ref. [20], as long as $\Gamma PL_{\text{eff}} \leq 0.2$ the effect of TPA and FCA remains small. In the above example, the nonlinear parameter $\Gamma = 2\pi n_2 / (\lambda A_{\text{eff}}) \simeq 30.7 \text{W}^{-1}\text{m}^{-1}$. The effective propagation length, L_{eff} , is determined through the cavity linewidth (FWHM = 20 GHz) and photon lifetime [$\tau = 1/(2\pi \text{FWHM}) \simeq 8 \text{ps}$] in such a cavity, and is given by $L_{\text{eff}} = c\tau/n_g \simeq 0.65 \text{mm}$. With $P = 0.1 \text{W}$, we estimate $\Gamma PL_{\text{eff}} \simeq 0.002$. At this ΓPL_{eff} level, we can safely ignore the nonlinear loss terms such as TPA and FCA.

Raman scattering in an SOI microring deserves some special attention, partly because of the ring geometry which mandates transformation of $\chi^{(3)}$ tensor components. Here we adopt the formalism in Ref. [23] to systematically derive the transformed $\chi^{(3)}$ tensor components for a microring resonator fabricated on Si (1 0 0) wafer whose coordinates are shown in Fig. 1(b). In the Cartesian coordinate system where $x = [1 \ 0 \ 0]$, $y = [0 \ 1 \ 0]$, $z = [0 \ 0 \ 1]$ are the crystallographic axes, the third-order nonlinear response function is given by (Eq. (39) in Ref. [23]):

$$R_{ijkl}^{(3)}(\tau) = \gamma_e \delta(\tau) \left[\frac{\sigma}{3} (\delta_{ij} \delta_{kl} + \delta_{ik} \delta_{jl} + \delta_{il} \delta_{jk}) + (1 - \sigma) \delta_{ij} \delta_{jk} \delta_{kl} \right] + \gamma_R h_R(\tau) (\delta_{ik} \delta_{jl} + \delta_{il} \delta_{jk} - 2\delta_{ij} \delta_{jk} \delta_{kl}). \quad (16)$$

Here γ_e (γ_R) is the electronic (Raman) part of the third-order nonlinearity, δ_{ij} is the Kronecker delta, $\delta(\tau)$ is the Dirac delta function, $h_R(\tau)$ is the Raman response function, and $\sigma \approx 1.27$ is the nonlinear anisotropy at 1550 nm [23].

The ring geometry requires that the nonlinear response function be transformed into the polar coordinate system, where $x = x$, $y = \rho \cos \theta$, $z = \rho \sin \theta$. The transformation matrix is given by

$$\begin{bmatrix} a'_x \\ a'_\rho \\ a'_\theta \end{bmatrix} = \begin{bmatrix} M_{xx} & M_{xy} & M_{xz} \\ M_{\rho x} & M_{\rho y} & M_{\rho z} \\ M_{\theta x} & M_{\theta y} & M_{\theta z} \end{bmatrix} \cdot \begin{bmatrix} a_x \\ a_y \\ a_z \end{bmatrix}, \quad (17)$$

where a_j is the unit vector along axis j , and the (un)primed notations represent the (Cartesian) polar coordinate. The matrix M is calculated to be:

$$\begin{bmatrix} M_{xx} & M_{xy} & M_{xz} \\ M_{\rho x} & M_{\rho y} & M_{\rho z} \\ M_{\theta x} & M_{\theta y} & M_{\theta z} \end{bmatrix} = \begin{bmatrix} 1 & 0 & 0 \\ 0 & \cos \theta & \sin \theta \\ 0 & -\frac{\sin \theta}{\rho} & \frac{\cos \theta}{\rho} \end{bmatrix}. \quad (18)$$

Tensor transformation obeys $R'_{qrst} = R_{ijkl}^{(3)} M_{qi} M_{rj} M_{sk} M_{tl}$, where Einstein summation convention is assumed. Using Eq. (18), we obtain the four nonlinear response components pertaining to the TE and TM modes in the polar coordinate system:

$$R'_{\rho\rho\rho\rho} = \gamma_e \delta(\tau) (\cos^4 \theta + \sin^4 \theta + 2\sigma \sin^2 \theta \cos^2 \theta) + 4\gamma_R h_R(\tau) \sin^2 \theta \cos^2 \theta, \quad (19)$$

$$R'_{xxxx} = \gamma_e \delta(\tau), \quad (20)$$

$$R'_{x\rho\rho x} = R'_{\rho x x \rho} = \frac{\sigma}{3} \gamma_e \delta(\tau) + \gamma_R h_R(\tau). \quad (21)$$

One can see that Raman component is absent only for the TM-TM process (corresponding to R'_{xxxx}), and is present for all other processes (TM-TE, TE-TM, TE-TE). The design rule for avoiding Raman scattering can therefore be summarized as: (i) for TM pump, there is no TE resonance 15.6 THz away; or (ii) for TE pump, there is neither a TE nor TM resonance 15.6 THz away. Both rules are satisfied, for example, with the design of $R_1 = 8 \mu\text{m}$. Calculations show that neither TM-pump nor TE-pump-derived Raman Stokes wave occurs near any TE or TM resonances for this particular design. It is not the case, however, for the design with $R_1 = 10 \mu\text{m}$, where the TE-pump-derived Raman Stokes wave occurs too close to a TE resonance (less than 120 GHz away), violating the above rule (ii). It can still be used to enhance FWM photon pairs with a TM-pump, since its Raman Stokes wave occurs far enough from any TE resonances.

4. Straight cavities

For a straight cavity, its cavity length is fixed (i.e., independent of the mode number) in contrast to the varying cavity lengths for WGM modes. Therefore, we can calculate the resonances of a straight cavity by numerically solving the following nonlinear equation:

$$n_g L = M \lambda, \quad (22)$$

where M is the mode number, λ is the resonant wavelength, L is the cavity length, and n_g is the group index for the resonant wavelength in a straight waveguide [such as the one shown in Fig. 3(a)]. Taking into account $n_g = c \frac{dk}{d\omega}$ and $\lambda = 2\pi c / \omega$, Eq. (22) is reduced to

$$\omega \frac{dk}{d\omega} = \frac{2\pi M}{L}. \quad (23)$$

Resonant frequency of mode number M is obtained by numerically solving Eq. (23). Following the discussions in Section 3, we calculate the frequency mismatch of a straight cavity (cross

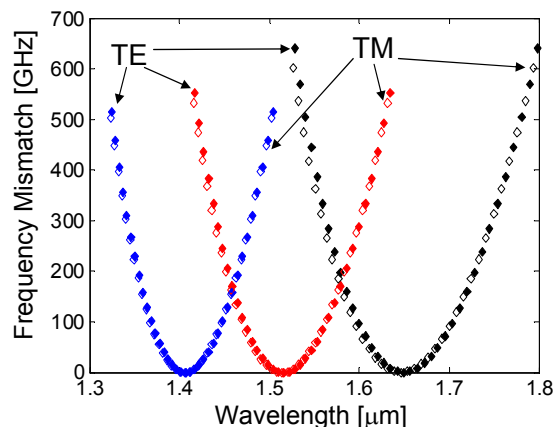


Fig. 6. Frequency mismatch in a straight cavity for quasi-TE modes with $\lambda_p = 1.407 \mu\text{m}$ (solid blue), $1.516 \mu\text{m}$ (solid red), and $1.649 \mu\text{m}$ (solid black), and quasi-TM modes with $\lambda_p = 1.405 \mu\text{m}$ (hollow blue), $1.514 \mu\text{m}$ (hollow red), and $1.646 \mu\text{m}$ (hollow black).

dimension 750 nm by 750 nm and length $L = 100 \mu\text{m}$ with air top cladding) for both its quasi-TE and quasi-TM modes, as shown in Fig. 6.

It can be seen that the frequency mismatch *always* grows with mode separation, independent of the pump wavelength. This is in stark contrast with the microring case, where there is a flat dispersion-compensated frequency range for a properly-chosen pump wavelength (i.e., λ_{opt}). For the straight-cavity case, there are only a few resonant modes for which the frequency mismatch is below the cavity linewidth (20 GHz in our case). For those modes cavity-enhanced FWM still play a role. One can, of course, broaden the cavity linewidth to incorporate more dispersion-compensated modes, at the expense of a lower cavity Q . We have also explored several other cross-sectional dimensions of a straight cavity, and find that the same conclusion holds: In general, for a given cavity linewidth, the straight-cavity design is inferior to its ring-cavity alternative for enhancing FWM.

5. Conclusion

We have developed a quantum mechanical theory for the two-photon state generated via spontaneous FWM inside an SOI micro-cavity. The two-photon state is shown to be a frequency-bin entangled comb of photon pairs. We have also provided practical design principles for SOI microring-based photon-pair sources through extensive numerical simulations. More specifically, an SOI microring with an inner radius of $8 \mu\text{m}$ can output an entangled photon comb of 21 pairwise-correlated peaks (42 comb lines) spanning from $1.3 \mu\text{m}$ to $1.8 \mu\text{m}$. Microring resonators are found to be superior than straight cavities at enhancing FWM photon-pair generation, as the latter lack a wide dispersion-compensated wavelength region. Such integrated-optic devices are a building block of future quantum integrated circuits, which consist of passive waveguides, interferometers, modulators, and quantum logic gates etc., all integrated on a single chip. We believe Silicon-on-Insulator is the platform of choice. Future research is aimed at fabricating the proposed devices, and experimentally demonstrating cavity-enhanced frequency-bin entangled photon-pair comb generation in SOI microring resonators.

Official contribution of the National Institute of Standards and Technology; not subject to copyright in the United States.